LAWRENCE
LIVERMORE
NATIONAL
LABORATORY

LLNL-JRNL-768579

Using Ultramicroporous Carbon for the Selective Removal of Nitrate with Capacitive Deionization

S. A. Hawks, M. R. Ceron, T. A. Pham, C. Zhan, C. K. Loeb, D. Mew, A. Deinhart, B. C. Wood, J. G. Santiago, M. Stadermann, P. G. Campbell

February 28, 2019

Environmental Science and Technology

Disclaimer

Using Ultramicroporous Carbon for the Selective Removal of Nitrate with Capacitive Deionization

Steven A. Hawks,[†] Maira R. Cerón,[†] Tuan Anh Pham,[†] Cheng Zhan,[†] Colin K. Loeb,[†] Daniel Mew,[†] Amanda Deinhart,[†] Brandon C. Wood,[†] Juan G. Santiago,[‡] Michael Stadermann,[†] and Patrick G. Campbell[†]**

[‡]Department of Mechanical Engineering, Stanford University, Stanford, CA 94305, United States
[†]Lawrence Livermore National Laboratory, 7000 East Avenue, Livermore, CA 94550, United States

E-mail: stadermann3@llnl.gov
E-mail: campbell82@llnl.gov

The contamination of water resources with nitrate is a growing and significant problem. Here we report the use of ultramicroporous carbon (average pore size <1 nm) as a capacitive deionization (CDI) electrode for selectively removing nitrate from an anion mixture. Through moderate activation, we achieve a pore-size distribution consisting almost exclusively of narrow (<1 nm) slit pores that are perfectly suited for adsorbing the planar, weakly hydrated, nitrate molecule. Cyclic voltammetry reveals an enhanced capacitance for nitrate when compared to chloride as well as significant ion sieving effects when sulfate is used as the electrolyte anion. We measure exceptionally high selectivities (S) of both nitrate over sulfate ($S_{NO3/SO4}$ = 18 ± 5) and nitrate over chloride ($S_{NO3/Cl}$ = 5 ± 1) when performing a constant voltage CDI separation on 3.33 mM/3.33 mM/1.67 mM Cl/NO_3/SO_4 water. We use molecular dynamics simulations to better understand why the pore-size distribution has such a dramatic impact on the electrosorption selectivity of these ions.

INTRODUCTION

Capacitive desalination is a water treatment technology of emergent interest for use in treating low salinity brackish waters.[1–4] In addition to general salinity reduction,[5–9] a particular area of interest in CDI research is the selective removal of specific ionic contaminants for increased energy efficiency and effective removal capacity.[10–16] One of the major contaminants of interest in CDI research is nitrate,[17–24] which is regulated by the US Environmental Protection Agency to a maximum contaminant level in drinking water of 10 mg/L at N or 0.7 mM as NO_3.[17] The concentration of nitrate in groundwater is increasing by a reported 1-3 mg/L/yr due to a number of factors,[17] making the development of effective treatment methods increasingly important.

From the standpoint of CDI, nitrate removal presents a unique opportunity due to its particular solvation properties and the fact that CDI typically relies on activated carbon electrodes to electrosorb ions.[25,26] Specifically, the nitrate molecule is planar and weakly hydrated,[27] which makes it ideal for

LLNL-JRNL-768579

insertion into slit-shaped carbon micropores.[28,29] It is well known that microporous activated carbon can show significant ion sieving effects when the solvated ion is too large compared to the micropore-size distribution.[30–35] We note that the effective ion "size" depends on the solvation structure, including how strongly the ion is solvated. Given these considerations, it is reasonable to expect that a pore-size distribution of exclusively narrow pores (<1 nm) would screen-out common unwanted ions in favor of selectively adsorbing nitrate. Such an approach is expected to be highly effective because divalent species would be strongly rejected due to their larger hydrated size and tightly-bound solvation shell.[27,36] In general, if the selective adsorption of any monovalent species is desired with CDI, it is critical to avoid competition from divalent species, as they are typically present in real waters and are expected to preferentially adsorb due to their higher valence.[13,37]

In this work, we successfully realize the idea of achieving highly selective nitrate adsorption ($S_{NO3/X}$ > 5) by utilizing ultramicroporous hierarchical carbon aerogel monolith (μHCAM) electrodes with a tight micropore size distribution consisting mainly of pores <1 nm in width. To demonstrate selectivity, we chose chloride and sulfate as interferant species because they are commonly found in real waters and, together with nitrate, span a large cross section of hydrated ion properties (see Hofmeister series).[38] Through cyclic voltammetry, gas adsorption, and electrochemical impedance spectroscopy measurements, we provide evidence that the mechanism of selectivity is ion sieving. Through detailed first-principles molecular dynamics simulations, we further conclude that the unique, disk-like, shape of the nitrate molecule along with its weak hydration shell is the likely reason behind the high selectivity values that we observe.

▪ MATERIALS AND METHODS

Ultramicroporous hierarchical carbon aerogel monoliths (μHCAM) were synthesized by the method of Baumann et al.[39] The aerogel was carbonized at 950 °C for 3 h under N_2, and subsequently activated for 1h at 950 °C under CO_2 flow. Scanning electron microscope (SEM) micrographs were taken in a Phenom ProX desktop platform (Figure **1**).

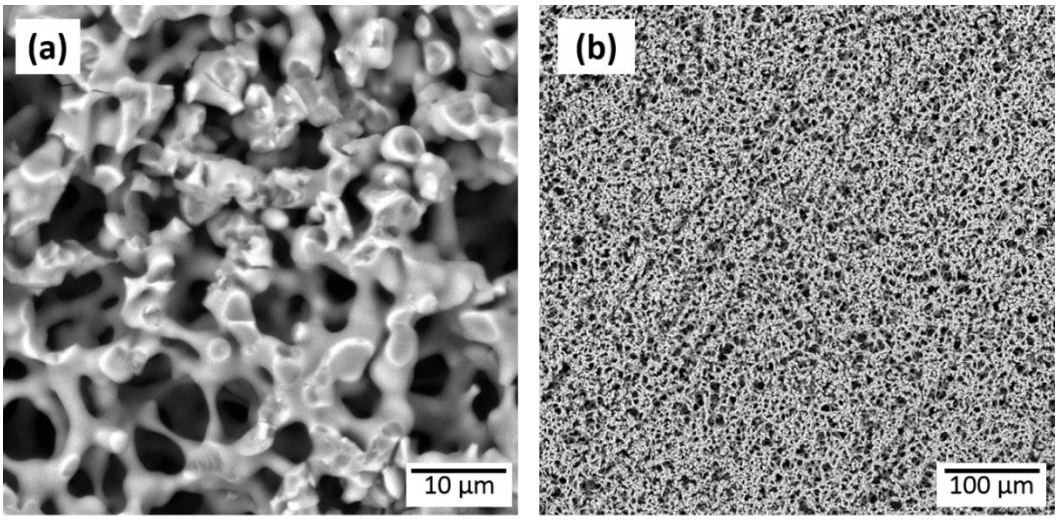

Figure 1. SEM micrographs of the cross section of the µHCAM electrodes after carbonization and activation at high (a) and low (b) magnifications.

Ion sieving effects were measured by cyclic voltammetry in pure solutions of 50 mM NaCl and $NaNO_3$, and 25 mM Na_2SO_4 using two sheets of µHCAMs synthesized as described above.[39] These electrodes had a face area of 5.6 cm^2 with an average thickness of 470 µm. The material had a mass density of 0.50 g/cm^3 and an approximate total surface area of 1084 m^2/g by DFT analysis (862 m^2/g BET) as measured from of N_2 adsorption experiments (Micrometrics). Assuming a carbon density of 1.95 g/cm^3 and a microporosity of 0.3 cm^3/g, the measured density implies an average total porosity of 74% with approximately 59% attributable to macropores and 15% attributable to micropores. The two carbon aerogel electrodes were separated by a 90 µm thick 2.5 cm by 3.5 cm non-conductive polyester mesh (McMaster-Carr, 9218T73), with an estimated porosity of 34%. For contacts, custom clippers with four titanium wires were used.

For selective ion removal measurements, a flow-through (fteCDI) cell was assembled using µHCAMs. The dimensions of the electrodes were 4 cm by 5.6 cm (projected face area of 22.4 cm^2)[5] with an average thickness of 475 µm. The material had a mass density of 0.55 g/cm^3, giving an average total porosity of 72% with approximately 55% attributable to macropores and 17% attributable to micropores. For an electrode separator, we used 4.5 cm by 6 cm coffee filter paper that was 150 µm thick. For contacts, four strips of 30 µm thick 99.6% titanium foil (Solution Materials LLC) were inserted into the cell.[40] The

electrodes and separator were stacked between laser-roughened 0.1 mm thick acrylic endplates with ports cut out for fluid flow. The cell was sealed with a UV-cure epoxy and clamped to reduce contact resistance.[40]

The resistance and capacitance of the cell was characterized by electrochemical impedance (Z) spectroscopy (EIS) and cyclic voltammetry (CV). During electrochemical tests, the cell was fed with a constant flow of 3 mL/min solution (see SI; BioLogic VSP-300 potentiostat) using a peristaltic pump (Watson Marlow, Falmouth, Cornwall UK) in closed-loop circulation with a 1 L reservoir continuously purged with water-vapor saturated nitrogen. For EIS, we applied a sinusoidal potential perturbation with amplitude of 10 mV and scanned over a frequency range from 700 kHz to 5 mHz at 0 V DC bias immediately after discharging the cell for several minutes at short circuit.

The desalination performance of the cell was tested under constant voltage operation using a Keithley 2602B SourceMeter (Tektronix Inc.), charge voltage 0.4, 0.6, 0.8 and 1.0 V, discharge voltage 0 V, flow rate 3 mL/min, and charge/discharge time ≥25 min. Ion selectivity was measured for a mixture of 3.33 mM of NaCl, 3.33 mM of $NaNO_3$ and 1.67 mM Na_2SO_4. All salts were ACS reagent grade (Sigma-Aldrich). The water used to make all solutions was Milli-Q ultrapure 18.2 MΩ-cm. To monitor the effluent concentration, we used a flow-through conductivity sensor (Horiba 3574-10C) installed downstream of the CDI cell. The sensor was kept close to the effluent port and attached to a narrow 1.59 mm inner-diameter tube. The sensor was multi-point calibrated with NIST traceable KCl conductivity standards corrected for ambient temperature (Oakton Instruments, Vernon Hills, IL).

Individual anion concentrations (chloride, nitrate, and sulfate) were measured by ion chromatography (IC). A Dionex ICS-5000 ion chromatograph with an Ion Pac AG18 2x50 mm guard column and Ion Pac AS18 2x250 mm analytical column were used. The mobile phase was KOH and autogenerated via a Dionex EGC 500 KOH eluent generator cartridge (Thermo/Dionex #075778). The eluent program was 2mM to 50mM in a two-stage ramp. The column and detector temperature was 35°C. The detector suppressor was an electrolytically regenerated suppressor with 18 MΩ laboratory grade water as the regeneration fluid. The regenerated suppressor was supplied at 0.25 mL/min, the suppressor current

setting was 31 mA, and the standard injection volume was 5 μL. Calibration solutions were commercially purchased.

In order to provide a better understanding of the experimental data, we carried out first-principles molecular dynamics simulations of chloride, nitrate, and sulfate ions dissolved in bulk water. These simulations provide insights into the hydration structure of each ion with high fidelity, including geometry and solvation strength, which can be directly related to the ion selectivity observed in the experiments. Specifically, the salt solutions were modeled by periodic cubic cells consisting of 63 water molecules and a single solvated ion, with the excess charge compensated by a uniform background charge. The size of the cells was chosen to yield the experimental density of liquid water under ambient conditions. Our first-principles simulations were carried out using Born-Oppenheimer molecular dynamics with the Qbox code,[41] with the interatomic force derived from density functional theory (DFT) and the Perdew, Burke, and Ernzerhof (PBE) approximation for the exchange-correlation energy functional.[42] The interaction between valence electrons and ionic cores was represented by norm-conserving pseudopotentials,[43] and the electronic wave functions were expanded in a plane-wave basis set truncated at a cutoff energy of 85 Ry. All hydrogen atoms were replaced with deuterium to maximize the allowable time step, which was chosen to be 10 au. The equilibration runs were carried out at an elevated temperature of T = 400 K in order to recover the experimental water structure and diffusion, while providing a good description of the ion solvation at room temperature.[44,45] For the analysis of structural properties, the statistics were collected over 45 ps microcanonical simulations after an equilibration run of 15 ps. Together with the first-principles molecular dynamics simulations, the reference interaction site method was employed to estimate the hydration solvation energy of the ions.[46] In these calculations, the simple point charge (SPC) model was applied to water, and the optimized potentials for the liquid simulations all-atom force field were used to describe the interaction between ions and water molecules.[47]

▪ RESULTS AND DISCUSSION

Hydrated Ion Properties

In order to establish a baseline for the discussion of our experimental data, we summarize the first-principles results of the solvation structure of chloride, nitrate, and sulfate ions in bulk water. Figure **2** presents the radial distribution functions (RDF) between oxygen atoms of water molecules and the anions. For nitrate and sulfate, we choose to compute the RDF between water oxygens and the nitrogen and sulfur atom of the ions, respectively. The results indicate that the hydrated chloride ion is significantly smaller (15-17%) than both the nitrate or sulfate ion in terms of the proximity of the nearest water molecules. Interestingly, from the standpoint of the RDF, a hydrated nitrate ion is similar in size to a sulfate ion but with a different average number of water molecules in the hydration shell. Specifically, by integrating the radial distribution functions up to the corresponding first minimum, we find an oxygen coordination number of 13.6 and 10.5 for nitrate and sulfate ions, respectively. The simulations reveal a significant difference in hydration-shell geometry between the ions due to the fact that nitrate is a planar molecule,[28] while sulfate and chloride are essentially symmetrical in three-dimensions. Along these lines, Figure **3** visualizes the hydration shell of sulfate, chloride, and nitrate, showing that chloride and sulfate have a more symmetric, spherical-like, hydration shells whereas nitrate is solvated in a disk-like manner. We hypothesize that this disk-like shape is critical to understanding why nitrate readily adsorbs into carbon slit pores.[28]

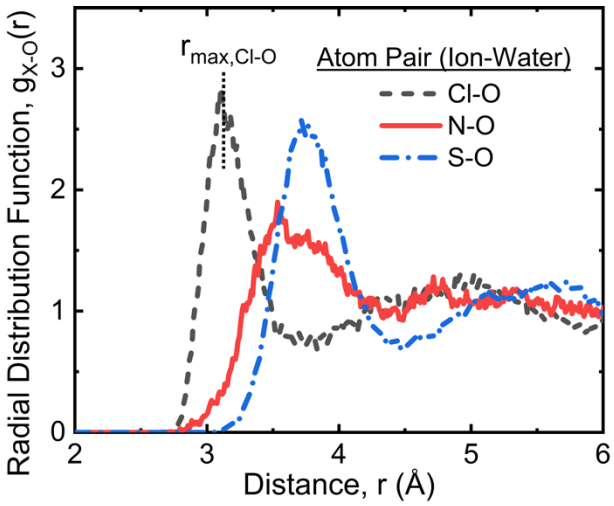

Figure 2. The calculated ion-oxygen radial distribution functions for chloride (Cl-O), nitrate (N-O), and sulfate (S-O) in bulk water.

Table 1. Ion Solvation Properties

Ion	$\Delta_{hyd}G_{calc}$* (kJ/mol)	$\Delta_{hyd}G_{exp}$* (kJ/mol) from Ref. 27	$r_{max,X-O}$ (Å)
NO_3^-	-333	-300	3.67 (N-O)
Cl^-	-340	-340	3.12 (Cl-O)
SO_4^{2-}	-1192	-1080	3.75 (S-O)

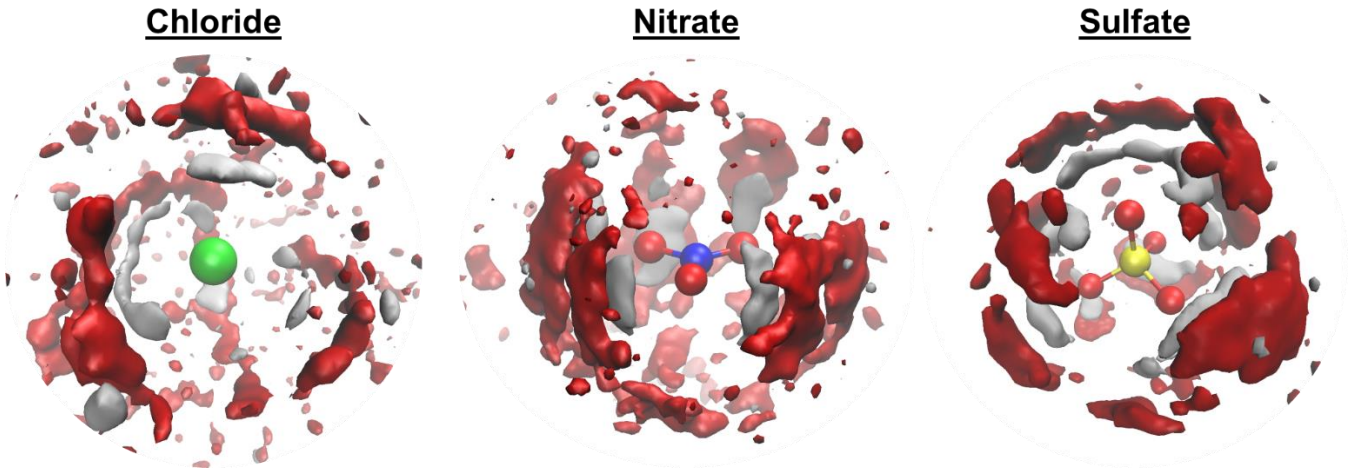

Figure 3. Spatial distribution functions of the hydration shell in Cartesian space of nitrate, chloride, and sulfate. The color key is as follows: red = oxygen, white/grey = hydrogen, green = chlorine, blue = nitrogen, and yellow = sulfur.

Another critical factor in understanding hydrated ion properties is the strength of the solvation shell, which has been discussed at length in the literature.[25–27,36] Both theory and experiment (Table 1) indicate a substantially larger standard molar Gibbs free energy of hydration for divalent sulfate (-1080 kJ/mol) when compared to monovalent nitrate (-300 kJ/mol) and chloride (-340 kJ/mol).[27] Interestingly, nitrate and chloride have a similar standard molar Gibbs free energy of hydration, with Cl^- being slightly more strongly solvated. Thus, given the difference in size and similarity in solvation shell strength, one might expect chloride to be preferentially adsorbed into confined pores over nitrate. However, we show below that the opposite is true, with the reason likely being related to the disk-like hydrated nitrate ion readily fitting into narrow carbon slit pores.

Pore-Size Distribution

Figure 4 shows the pore-size distribution as measured from N_2 gas sorption experiments for the μHCAM material studied here as well as that for Suss et al.,[48] which is a similar HCAM material but with different microporosity than that examined in this work. While CO_2 is the preferred gas for use in sorption measurements to quantify the microporosity of carbonaceous materials,[49] the two gases have been shown to yield similar results for ultramicroporous carbon.[35] Here we use the measured microporosity in cm^3/g as a proxy for degree of activation since furnace conditions are highly sensitive to experimental details (e.g., time, temperature, flow rate, tube diameter, loading, sample geometry, etc). Figure 4a gives insight into how the pore-size distribution evolves with more activation in these HCAM materials. Figure 2b shows the cumulative area for the material studied herein, which has a reasonable 85 F/g in 2 M NaCl capacitance and virtually all the micropores below 1 nm.

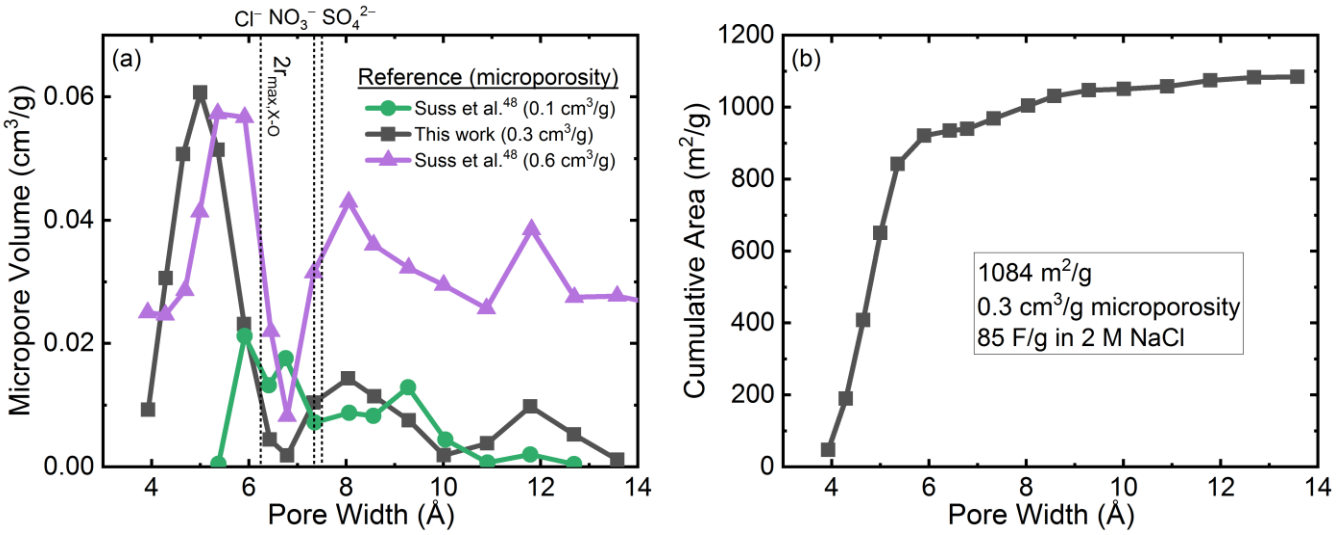

Figure 4: Pore size characteristics from N_2 adsorption measurements. (a) Micropore-size distribution as a function of slit pore width for this work and that of Suss et al.[48] (b) Cumulative micropore volume as a function of slit pore width for this work. The material used in this work and in Suss et al.[48] are processed identically according to Ref. 39 but are activated to different levels. The metrics indicated in (b) show that virtually all micropores in this work are well below 1 nm in width and the capacitance is reasonably high at 85 F/g. For reference, we mark the $2r_{max,X\text{-}O}$ position from Figure 2 and Table 1.

For HCAM material with no activation, Figure 4a confirms that there is limited accessible micropore area in general, whereas further activation up to 0.3 cm^3/g microporosity (this study) yields a large number of ~0.5 nm width pores. For a sense of scale, this peak would correspond to slit pores that have no more than one sheet of graphene removed from a local graphitic structure. Such a narrow and small-sized pore distribution is known to occur with moderately activated carbons.[50,51] Further activation to 0.6 cm^3/g

microporosity (triangles in Figure 4a) significantly increases the relative distribution of micropores between 0.4-1.4 nm. From the standpoint of ion sieving, the strongly ultramicroporous structure obtained here is ideal as there are a large number (1085 m^2/g) of small ~0.5 nm slit-like pores and very little porosity larger than 1 nm in width. In Figure 4a, we mark the locations of the approximate first peak position of the ion-oxygen radial distribution function for Cl^-, NO_3^-, and SO_4^{2-} taken from Table 1 and Figure **2**, indicating that such small pores are expected to show strong confinement effects for all the ions studied.

Ion Sieving

As expected from the pore-size distribution of our μHCAM material (Figure **4**), cyclic voltammetry (CV) measurements display significant ion sieving features when Na_2SO_4 is used as the electrolyte (Figure **5**). The signature feature of ion sieving is a pinching of the CV curve (reduction in capacitance) at larger absolute voltages where the sieved species should be adsorbed.[28] Such behavior is clearly observed in Figure **5**a, where the Na_2SO_4 electrolyte displays a significant reduction in capacitance, especially at higher absolute voltages, whereas NaCl and $NaNO_3$ show typical low-electrolyte-concentration CV behavior. Because the measurements were made on a symmetric 2-electrode cell, sieving is observed at both positive and negative bias. The observation of divalent ion sieving with activated carbon electrodes has been observed before,[28,35,52] where it is believed that the divalent species are too large and too strongly hydrated to access the small micropores.[25–27] The results in Figure **5**a are consistent with this picture, even showing a higher capacitance for the slightly more weakly hydrated monovalent NO_3^- (-300 kJ/mol) when compared to Cl^- (-340 kJ/mol).[27] Given the similarities of chloride and nitrate in effective hydrodynamic size (Figure 4a) and solvation energy, it is surprising that there is such a significant difference of capacitance in Figure **5**. We hypothesize that the difference in hydrated shape between chloride and nitrate is the deciding factor in determining accessibility to the micropores and therefore also measured capacitance.

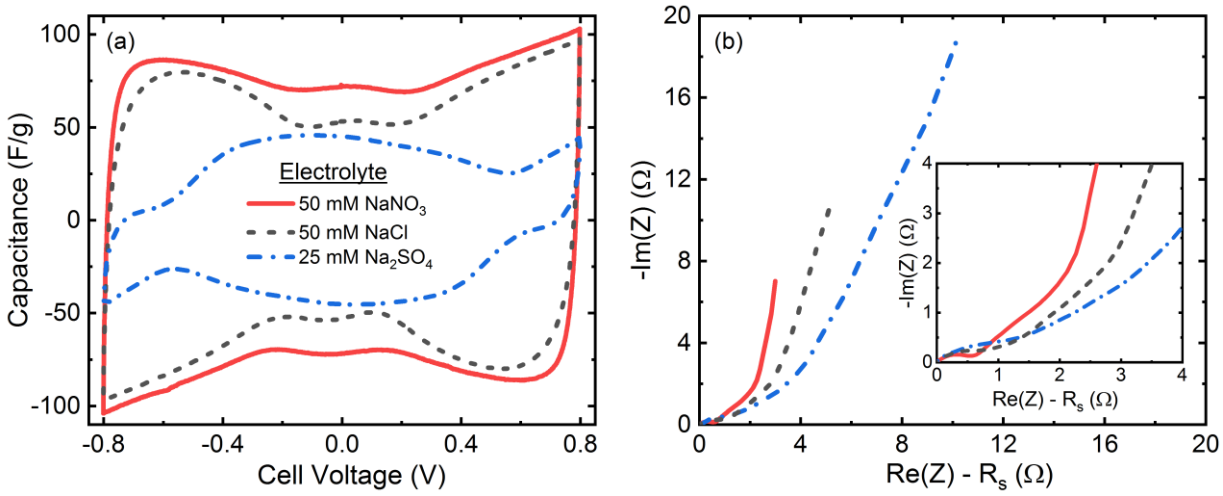

Figure 5: (a) Cyclic voltammograms of a symmetric 2-electrode cell taken at 0.5 mV/s in 50 mM $NaNO_3$, 50 mM NaCl, and 25 mM Na_2SO_4. Strong ion sieving is observed at larger voltages (>|0.2| V) for Na_2SO_4, but not for NaCl or $NaNO_3$. (b) Nyquist plots from EIS measurements (700 kHz-5 mHz) with the series resistance ($R_s \equiv$ Re(Z) @ Im(Z) = 0) subtracted from the real component. CV and EIS experimental details are described in the materials and methods section.

Figure **5**b presents EIS data for the corresponding CV curves in Figure **5**a taken from 700 kHz to 5 mHz at short circuit with the series resistance (R_s, here defined as Re(Z) @ Im(Z) = 0) subtracted from the real component. The significant differences in resistance are surprising given that at an ambient temperature of 22°C one would expect the electrolyte conductivities to be: 50 mM NaCl = 5.14 mS/cm, 50 mM $NaNO_3$ = 4.89 mS/cm, and 25 mM Na_2SO_3 = 4.55 mS/cm.[53] Thus, despite only a 12% difference in conductivity, the measured Re(Z) at 5 mHz is 340% larger for Na_2SO_3 when compared to $NaNO_3$. Furthermore, the trend in Re(Z) is opposite to the direction that would be expected from the conductivity of $NaNO_3$ vs. NaCl. Thus, we conclude that the EIS spectrum at short circuit is also impacted by micropore adsorption effects. Segalini et al.[31] witnessed similar EIS behavior when examining carbons with pore-size distributions that transitioned between sieving and non-sieving for a given electrolyte. It their work, it was found that the low frequency region of the Nyquist plot deviated more strongly from the expected vertical line when significant ion sieving effects were present, indicating non-ideal capacitive behavior.[31] A potential physical explanation for the observed differences in impedance can be found from the work of Suss et al.,[48] who concluded that materials with a significant storage-pore resistance would display a lower phase angle (<45°) at intermediate high frequencies (linear portion at low Re(Z) in Figure

5b inset). Indeed, the phase angle for $NaNO_3$ and NaCl in the Figure **5**b inset are exactly 45° in the intermediate high frequency linear regime, whereas the phase angle for Na_2SO_3 is significantly lower than 45° (~12-36°), suggesting a more significant storage-pore resistance.

Selective Adsorption with $Cl/NO_3/SO_4$ Mixtures.

With the ions and electrodes individually characterized, we measured the electrosorption selectivity of our μHCAM materials in a flow-through electrode CDI cell (Figure **6**). To do so, we used a 3.33 mM/3.33 mM/1.67 mM $NaCl/NaNO_3/Na_2SO_4$ feed solution and charged the cell at various constant voltages (0.4-1 V) under a constant flow rate (3 ml/min) while monitoring the effluent conductivity (Figure **6**a). Here we observed a highly unusual effluent curve, where the salinity initially decreased sharply, but was then followed by a rapid increase and subsequent second decrease (Figure **6**a). This anomalous increase in conductivity during the constant voltage charging phase was not present at low charging voltages (0.4 V) but was clearly visible for larger voltages (1 V). Such non-monotonic behavior is highly atypical for CDI effluent conductivity curves. We hypothesize that this is caused by a multi-step process: first the ions are adsorbed statistically (non-selectively), which corresponds to the initial sharp decrease in conductivity; second, at later times, the electrode self-corrects for undesirable concentration ratios of adsorbed species by rejecting unwanted ions (rise in conductivity) and replacing them with desirable species (second decrease in conductivity). Such a time-dependent selectivity is in qualitative agreement with the results and analysis of Zhao et al.,[13] who observed a similar effect with a mixture of Ca^{2+} and Na^{+}. In particular, Zhao et al.[13] noted that the modified Donnan model predicts non-specific adsorption during the early times of a charging phase, which is then followed by the replacement of undesirable ions (e.g., Na^{+}) with those that are preferentially adsorbed (e.g. Ca^{2+}). It appears that a similar phenomenon is occurring here, however further analysis actually reveals anti-selectivity for the divalent species (Figure **6**b,c).

After charging the cell at constant voltage and flow for an extended period of time (>25 min), we discharged the device at zero volts and collected the resulting concentrate, stopping once the cell current

density decayed to a low value (0.045 mA/cm^2). With the concentrate solution in hand, we were able to measure the ion concentration ratios that were adsorbed onto the electrodes during the charging phase with ion chromatography. Figure **6**b presents the resulting raw concentration values of nitrate, chloride, and sulfate in the collected concentrate solution. Surprisingly, by far the dominant adsorbed species was nitrate, followed by chloride, and then lastly by sulfate ($NO_3^- > Cl^- \gg SO_4^{2-}$). The sulfate concentration scarcely deviated from the feed (Figure **6**b), indicating that it was essentially not adsorbed. These results are consistent with the ion sieving results obtained above and indicate that ultramicroporous carbon can be used as a highly selective sorbent for nitrate and perhaps other weakly solvated planar ions even in the presence of divalent ions.[54]

The concentrate concentrations of Figure **6**b can be used to calculate the electrosorption selectivity of the device for one ion over another. In order to calculate these selectivity values, we modify the IUPAC selectivity coefficient for adsorbed ions, defining that

$$S_{A/B} = \frac{\frac{c_{ads,A}}{c_{ads,B}}}{\frac{c_{f,A}}{c_{f,B}}} \tag{1}$$

where $S_{A/B}$ is the selectivity coefficient for species A over species B, $c_{ads,A}$ is the adsorbed concentration of species A, $c_{ads,B}$ is the adsorbed concentration of species B, $c_{f,A}$ is the free concentration of species A, and $c_{f,B}$ is the free concentration of species B. For the purposes of this work, we ignore valence modifications to Eqn. (1) and rewrite it in terms of the excess concentration in the concentrate solution (Δc) and the feed concentration (c_{feed})

$$S_{A/B} = \frac{\frac{\Delta c_A}{\Delta c_B}}{\frac{c_{feed,A}}{c_{feed,B}}} \tag{2}$$

where $\Delta c_A = c_{c,A} - c_{feed,A}$ is the excess concentration of species A in the concentrate solution, $\Delta c_B = c_{c,B} - c_{feed,B}$ is the excess concentration of species B in the concentrate solution, $c_{feed,A}$ is the feed concentration of species A, $c_{feed,B}$ is the feed concentration of species B, $c_{c,A}$ is the concentration of species A in the concentrate solution (Figure **6**b), and $c_{c,B}$ is the concentration of species B in the concentrate solution (Figure **6**b).

Using Eqn. (2), we calculate the selectivities of nitrate over chloride ($S_{NO3/Cl}$) and nitrate over sulfate ($S_{NO3/SO4}$) and plot them as a function of cell voltage in Figure **6**c. Interestingly, we observe a weak voltage dependence of the selectivity, finding that $S_{NO3/Cl} = 5 \pm 1$ and $S_{NO3/SO4} = 18 \pm 5$ (Figure **6**c) independent of voltage. Of course, though, absolute removal does scale with voltage (Figure **6**a), which is another important factor to consider given that usually a target minimum concentration is desired (e.g. 10 ppm) and not a target selectivity. Thus, the fact that our nitrate selectivity remains high for larger removals (higher voltages) is another promising aspect of our results.

The observed nitrate selectivities are exceptionally high when compared to other CDI research, especially given that a divalent ion is present in addition to chloride.[12,17,19] Most importantly, these results are obtained without the need for specialized functionalization,[21,24] membranes,[23] or coatings;[18,20] and are measured in a relevant mixture with multivalent and chloride interferants. We conclude that our µHCAM electrodes are ideally suited for selectively removing nitrate from ion mixtures due to an excellent match between pore structure (narrow slits) and ion solvation properties (nitrate is a weakly solvated disc).[28] This work shows that the approach of tuning carbon electrode microporosity can be a highly effective way to achieve excellent electrosorptive selectivity. We note, though, that while these selectivities are encouraging, they must be realized in cycles with sufficient concentration reduction and throughput to have practical value. Thus, future work will seek to achieve practically valuable separations as well as further optimize nitrate selectivity by tuning pore size without sacrificing sorption capacity.

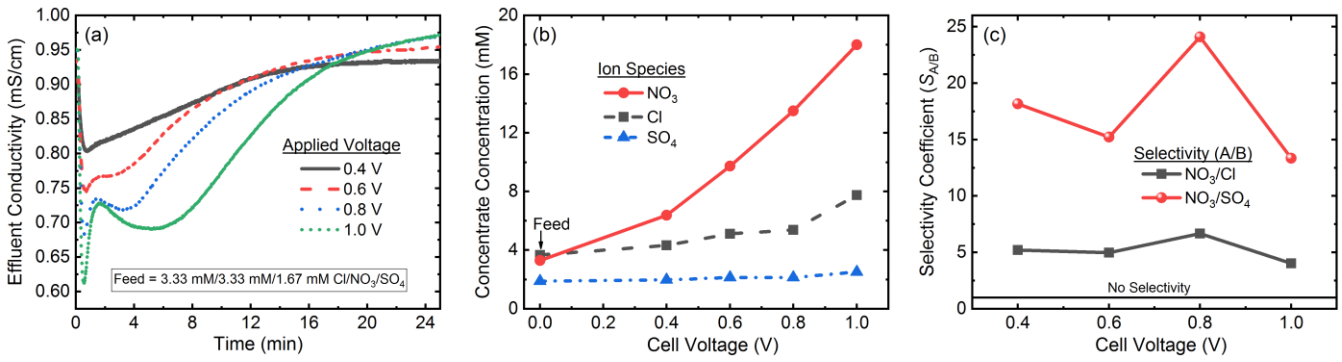

Figure 6: (a) Effluent conductivity profiles resulting from a constant-voltage charge with a 3.33 mM/3.33 mM/1.67 mM NaCl/$NaNO_3$/Na_2SO_4 feed solution flowed at 3 ml/min. The device had a face area of 22.4 cm^2. (b) Ion concentrations in the concentrate solution created from discharging the cell at zero volts after the

charging phase shown in (a). (c) The calculated nitrate/chloride and nitrate/sulfate selectivities from the results in (b).

■ ASSOCIATED CONTENT

Supporting Information. This material is available free of charge via the Internet at http://pubs.acs.org.

A brief statement in nonsentence format listing the contents of material supplied as Supporting Information should be included.

■ ACKNOWLEDGMENTS

Work at LLNL was performed under the auspices of the US DOE by LLNL under Contract DE-AC52-07NA27344. All work was supported by LLNL LDRD 18-ERD-024.

■ REFERENCES

(1) Suss, M. E.; Porada, S.; Sun, X.; Biesheuvel, P. M.; Yoon, J.; Presser, V. Water Desalination via Capacitive Deionization: What Is It and What Can We Expect from It? *Energy Environ. Sci.* **2015**, *8* (8), 2296–2319. https://doi.org/10.1039/C5EE00519A.

(2) Porada, S.; Zhao, R.; van der Wal, A.; Presser, V.; Biesheuvel, P. M. Review on the Science and Technology of Water Desalination by Capacitive Deionization. *Prog. Mater. Sci.* **2013**, *58* (8), 1388–1442. https://doi.org/10.1016/j.pmatsci.2013.03.005.

(3) Biesheuvel, P. M.; Bazant, M. Z.; Cusick, R. D.; Hatton, T. A.; Hatzell, K. B.; Hatzell, M. C.; Liang, P.; Lin, S.; Porada, S.; Santiago, J. G.; et al. Capacitive Deionization -- Defining a Class of Desalination Technologies. *arXiv* **2017**, 1–3.

(4) Tang, W.; Liang, J.; He, D.; Gong, J.; Tang, L.; Liu, Z.; Wang, D.; Zeng, G. Various Cell Architectures of Capacitive Deionization: Recent Advances and Future Trends. *Water Res.* **2019**, *150*, 225–251. https://doi.org/10.1016/j.watres.2018.11.064.

(5) Hawks, S. A.; Ramachandran, A.; Porada, S.; Campbell, P. G.; Suss, M. E.; Biesheuvel, P. M.; Santiago, J. G.; Stadermann, M. Performance Metrics for the Objective Assessment of Capacitive Deionization Systems. *Water Res.* **2018**. https://doi.org/10.1016/j.watres.2018.10.074.

(6) Ramachandran, A.; Hemmatifar, A.; Hawks, S. A.; Stadermann, M.; Santiago, J. G. Self Similarities in Desalination Dynamics and Performance Using Capacitive Deionization. *Water Res.* **2018**, *140*, 323–334. https://doi.org/10.1016/j.watres.2018.04.042.

(7) Ramachandran, A.; Hawks, S. A.; Stadermann, M.; Santiago, J. G. Frequency Analysis and Resonant Operation for Efficient Capacitive Deionization. *Water Res.* **2018**, *144*, 581–591. https://doi.org/10.1016/j.watres.2018.07.066.

(8) Hemmatifar, A.; Ramachandran, A.; Liu, K.; Oyarzun, D. I.; Bazant, M. Z.; Santiago, J. G. Thermodynamics of Ion Separation by Electrosorption. *arXiv* **2018**.

(9) Hemmatifar, A.; Palko, J. W.; Stadermann, M.; Santiago, J. G. Energy Breakdown in Capacitive Deionization. *Water Res.* **2016**, *104*, 303–311. https://doi.org/10.1016/j.watres.2016.08.020.

(10) Sigalov, S.; Levi, M. D.; Salitra, G.; Aurbach, D.; Jänes, A.; Lust, E.; Halalay, I. C. Selective Adsorption of Multivalent Ions into TiC-Derived Nanoporous Carbon. *Carbon N. Y.* **2012**, *50* (10), 3957–3960. https://doi.org/10.1016/j.carbon.2012.04.002.

(11) Seo, S. J.; Jeon, H.; Lee, J. K.; Kim, G. Y.; Park, D.; Nojima, H.; Lee, J.; Moon, S. H. Investigation on Removal of Hardness Ions by Capacitive Deionization (CDI) for Water Softening Applications. *Water Res.* **2010**, *44* (7), 2267–2275. https://doi.org/10.1016/j.watres.2009.10.020.

(12) Li, Y.; Zhang, C.; Jiang, Y.; Wang, T. J.; Wang, H. Effects of the Hydration Ratio on the Electrosorption Selectivity

of Ions during Capacitive Deionization. *Desalination* **2016**, *399*, 171–177. https://doi.org/10.1016/j.desal.2016.09.011.
(13) Zhao, R.; van Soestbergen, M.; Rijnaarts, H. H. M.; van der Wal, A.; Bazant, M. Z.; Biesheuvel, P. M. Time-Dependent Ion Selectivity in Capacitive Charging of Porous Electrodes. *J. Colloid Interface Sci.* **2012**, *384* (1), 38–44. https://doi.org/10.1016/j.jcis.2012.06.022.
(14) Dykstra, J. E.; Dijkstra, J.; Van der Wal, A.; Hamelers, H. V. M.; Porada, S. On-Line Method to Study Dynamics of Ion Adsorption from Mixtures of Salts in Capacitive Deionization. *Desalination* **2016**, *390*, 47–52. https://doi.org/10.1016/j.desal.2016.04.001.
(15) Hassanvand, A.; Chen, G. Q.; Webley, P. A.; Kentish, S. E. A Comparison of Multicomponent Electrosorption in Capacitive Deionization and Membrane Capacitive Deionization. *Water Res.* **2018**, *131*, 100–109. https://doi.org/10.1016/j.watres.2017.12.015.
(16) Su, X.; Tan, K.-J.; Elbert, J.; Rüttiger, C.; Gallei, M.; Jamison, T. F.; Hatton, T. A. Asymmetric Faradaic Systems for Selective Electrochemical Separations. *Energy Environ. Sci.* **2017**, *10* (5), 1272–1283. https://doi.org/10.1039/C7EE00066A.
(17) Uzun, H. I.; Debik, E. Economical Approach to Nitrate Removal via Membrane Capacitive Deionization. *Sep. Purif. Technol.* **2019**, *209*, 776–781. https://doi.org/10.1016/j.seppur.2018.09.037.
(18) Kim, Y.-J.; Choi, J.-H. Selective Removal of Nitrate Ion Using a Novel Composite Carbon Electrode in Capacitive Deionization. *Water Res.* **2012**, *46* (18), 6033–6039. https://doi.org/10.1016/j.watres.2012.08.031.
(19) Lado, J. J.; Pérez-Roa, R. E.; Wouters, J. J.; Tejedor-Tejedor, M. I.; Federspill, C.; Ortiz, J. M.; Anderson, M. A. Removal of Nitrate by Asymmetric Capacitive Deionization. *Sep. Purif. Technol.* **2017**, *183*, 145–152. https://doi.org/10.1016/j.seppur.2017.03.071.
(20) Yeo, J.-H.; Choi, J.-H. Enhancement of Nitrate Removal from a Solution of Mixed Nitrate, Chloride and Sulfate Ions Using a Nitrate-Selective Carbon Electrode. *Desalination* **2013**, *320*, 10–16. https://doi.org/10.1016/j.desal.2013.04.013.
(21) Oyarzun, D. I.; Hemmatifar, A.; Palko, J. W.; Stadermann, M.; Santiago, J. G. Adsorption and Capacitive Regeneration of Nitrate Using Inverted Capacitive Deionization with Surfactant Functionalized Carbon Electrodes. *Sep. Purif. Technol.* **2018**, *194*, 410–415. https://doi.org/10.1016/j.seppur.2017.11.027.
(22) Tang, W.; Kovalsky, P.; He, D.; Waite, T. D. Fluoride and Nitrate Removal from Brackish Groundwaters by Batch-Mode Capacitive Deionization. *Water Res.* **2015**, *84*, 342–349. https://doi.org/10.1016/j.watres.2015.08.012.
(23) Kim, Y.-J.; Kim, J.-H.; Choi, J.-H. Selective Removal of Nitrate Ions by Controlling the Applied Current in Membrane Capacitive Deionization (MCDI). *J. Memb. Sci.* **2013**, *429*, 52–57. https://doi.org/10.1016/j.memsci.2012.11.064.
(24) Oyarzun, D. I.; Hemmatifar, A.; Palko, J. W.; Stadermann, M.; Santiago, J. G. Ion Selectivity in Capacitive Deionization with Functionalized Electrode: Theory and Experimental Validation. *Water Res. X* **2018**, *1*, 100008. https://doi.org/10.1016/j.wroa.2018.100008.
(25) Tansel, B. Significance of Thermodynamic and Physical Characteristics on Permeation of Ions during Membrane Separation: Hydrated Radius, Hydration Free Energy and Viscous Effects. *Sep. Purif. Technol.* **2012**, *86*, 119–126. https://doi.org/10.1016/j.seppur.2011.10.033.
(26) Tansel, B.; Sager, J.; Rector, T.; Garland, J.; Strayer, R. F.; Levine, L.; Roberts, M.; Hummerick, M.; Bauer, J. Significance of Hydrated Radius and Hydration Shells on Ionic Permeability during Nanofiltration in Dead End and Cross Flow Modes. *Sep. Purif. Technol.* **2006**, *51* (1), 40–47. https://doi.org/10.1016/j.seppur.2005.12.020.
(27) Marcus, Y. Thermodynamics of Solvation of Ions. Part 5.—Gibbs Free Energy of Hydration at 298.15 K. *J. Chem. Soc., Faraday Trans.* **1991**, *87* (18), 2995–2999. https://doi.org/10.1039/FT9918702995.
(28) Eliad, L.; Salitra, G.; Soffer, A.; Aurbach, D. Ion Sieving Effects in the Electrical Double Layer of Porous Carbon Electrodes: Estimating Effective Ion Size in Electrolytic Solutions. *J. Phys. Chem. B* **2001**, *105* (29), 6880–6887. https://doi.org/10.1021/jp010086y.
(29) Kalluri, R. K.; Biener, M. M.; Suss, M. E.; Merrill, M. D.; Stadermann, M.; Santiago, J. G.; Baumann, T. F.; Biener, J.; Striolo, A. Unraveling the Potential and Pore-Size Dependent Capacitance of Slit-Shaped Graphitic Carbon Pores in Aqueous Electrolytes. *Phys. Chem. Chem. Phys.* **2013**, *15* (7), 2309. https://doi.org/10.1039/c2cp43361c.
(30) Lin, R.; Taberna, P. L.; Chmiola, J.; Guay, D.; Gogotsi, Y.; Simon, P. Microelectrode Study of Pore Size, Ion Size, and Solvent Effects on the Charge/Discharge Behavior of Microporous Carbons for Electrical Double-Layer Capacitors. *J. Electrochem. Soc.* **2009**, *156* (1), A7. https://doi.org/10.1149/1.3002376.
(31) Segalini, J.; Daffos, B.; Taberna, P. L.; Gogotsi, Y.; Simon, P. Qualitative Electrochemical Impedance Spectroscopy Study of Ion Transport into Sub-Nanometer Carbon Pores in Electrochemical Double Layer Capacitor Electrodes. *Electrochim. Acta* **2010**, *55* (25), 7489–7494. https://doi.org/10.1016/j.electacta.2010.01.003.
(32) Shilina, Y.; Levi, M. D.; Dargel, V.; Aurbach, D.; Zavorine, S.; Nucciarone, D.; Humeniuk, M.; Halalay, I. C. Ion Size to Pore Width Ratio as a Factor That Determines the Electrochemical Stability Window of Activated Carbon Electrodes. *J. Electrochem. Soc.* **2013**, *160* (4), A629–A635. https://doi.org/10.1149/2.058304jes.
(33) Salitra, G.; Soffer, A.; Eliad, L.; Cohen, Y.; Aurbach, D. Carbon Electrodes for Double-Layer Capacitors I. Relations Between Ion and Pore Dimensions. *J. Electrochem. Soc.* **2000**, *147* (7), 2486. https://doi.org/10.1149/1.1393557.
(34) Levi, M. D.; Levy, N.; Sigalov, S.; Salitra, G.; Aurbach, D.; Maier, J. Electrochemical Quartz Crystal Microbalance

(EQCM) Studies of Ions and Solvents Insertion into Highly Porous Activated Carbons. *J. Am. Chem. Soc.* **2010**, *132* (38), 13220–13222. https://doi.org/10.1021/ja104391g.
(35) Lorrmann, V.; Reichenauer, G.; Weber, C.; Pflaum, J. Electrochemical Double-Layer Charging of Ultramicroporous Synthetic Carbons in Aqueous Electrolytes. *Electrochim. Acta* **2012**, *86*, 232–240. https://doi.org/10.1016/j.electacta.2012.04.115.
(36) Marcus, Y. Effect of Ions on the Structure of Water: Structure Making and Breaking. *Chem. Rev.* **2009**, *109* (3), 1346–1370. https://doi.org/10.1021/cr8003828.
(37) Suss, M. E. Size-Based Ion Selectivity of Micropore Electric Double Layers in Capacitive Deionization Electrodes. *J. Electrochem. Soc.* **2017**, *164* (9), E270–E275. https://doi.org/10.1149/2.1201709jes.
(38) ZHANG, Y.; CREMER, P. Interactions between Macromolecules and Ions: The Hofmeister Series. *Curr. Opin. Chem. Biol.* **2006**, *10* (6), 658–663. https://doi.org/10.1016/j.cbpa.2006.09.020.
(39) Baumann, T. F.; Worsley, M. A.; Han, T. Y.-J.; Satcher, J. H. High Surface Area Carbon Aerogel Monoliths with Hierarchical Porosity. *J. Non. Cryst. Solids* **2008**, *354* (29), 3513–3515. https://doi.org/10.1016/j.jnoncrysol.2008.03.006.
(40) Hawks, S. A.; Knipe, J. M.; Campbell, P. G.; Loeb, C. K.; Hubert, M. A.; Santiago, J. G.; Stadermann, M. Quantifying the Flow Efficiency in Constant-Current Capacitive Deionization. *Water Res.* **2018**, *129*, 327–336. https://doi.org/10.1016/j.watres.2017.11.025.
(41) Gygi, F. Architecture of Qbox: A Scalable First-Principles Molecular Dynamics Code. *IBM J. Res. Dev.* **2008**, *52* (1.2), 137–144. https://doi.org/10.1147/rd.521.0137.
(42) Perdew, J. P.; Burke, K.; Ernzerhof, M. Generalized Gradient Approximation Made Simple. *Phys. Rev. Lett.* **1996**, *77* (18), 3865–3868. https://doi.org/10.1103/PhysRevLett.77.3865.
(43) Schlipf, M.; Gygi, F. Optimization Algorithm for the Generation of ONCV Pseudopotentials. *Comput. Phys. Commun.* **2015**, *196*, 36–44. https://doi.org/10.1016/j.cpc.2015.05.011.
(44) Pham, T. A.; Mortuza, S. M. G.; Wood, B. C.; Lau, E. Y.; Ogitsu, T.; Buchsbaum, S. F.; Siwy, Z. S.; Fornasiero, F.; Schwegler, E. Salt Solutions in Carbon Nanotubes: The Role of Cation−π Interactions. *J. Phys. Chem. C* **2016**, *120* (13), 7332–7338. https://doi.org/10.1021/acs.jpcc.5b12245.
(45) Pham, T. A.; Ogitsu, T.; Lau, E. Y.; Schwegler, E. Structure and Dynamics of Aqueous Solutions from PBE-Based First-Principles Molecular Dynamics Simulations. *J. Chem. Phys.* **2016**, *145* (15), 154501. https://doi.org/10.1063/1.4964865.
(46) Nishihara, S.; Otani, M. Hybrid Solvation Models for Bulk, Interface, and Membrane: Reference Interaction Site Methods Coupled with Density Functional Theory. *Phys. Rev. B* **2017**, *96* (11), 115429. https://doi.org/10.1103/PhysRevB.96.115429.
(47) Kaminski, G. A.; Friesner, R. A.; Tirado-Rives, J.; Jorgensen, W. L. Evaluation and Reparametrization of the OPLS-AA Force Field for Proteins via Comparison with Accurate Quantum Chemical Calculations on Peptides †. *J. Phys. Chem. B* **2001**, *105* (28), 6474–6487. https://doi.org/10.1021/jp003919d.
(48) Suss, M. E.; Baumann, T. F.; Worsley, M. A.; Rose, K. A.; Jaramillo, T. F.; Stadermann, M.; Santiago, J. G. Impedance-Based Study of Capacitive Porous Carbon Electrodes with Hierarchical and Bimodal Porosity. *J. Power Sources* **2013**, *241*, 266–273. https://doi.org/10.1016/j.jpowsour.2013.03.178.
(49) Thommes, M.; Kaneko, K.; Neimark, A. V.; Olivier, J. P.; Rodriguez-Reinoso, F.; Rouquerol, J.; Sing, K. S. W. Physisorption of Gases, with Special Reference to the Evaluation of Surface Area and Pore Size Distribution (IUPAC Technical Report). *Pure Appl. Chem.* **2015**, *87* (9–10), 1051–1069. https://doi.org/10.1515/pac-2014-1117.
(50) Koresh, J.; Soffer, A. Study of Molecular Sieve Carbons. Part 1.—Pore Structure, Gradual Pore Opening and Mechanism of Molecular Sieving. *J. Chem. Soc. Faraday Trans. 1 Phys. Chem. Condens. Phases* **1980**, *76* (2), 2457. https://doi.org/10.1039/f19807602457.
(51) Dubinin, M. .; Stoeckli, H. . Homogeneous and Heterogeneous Micropore Structures in Carbonaceous Adsorbents. *J. Colloid Interface Sci.* **1980**, *75* (1), 34–42. https://doi.org/10.1016/0021-9797(80)90346-X.
(52) Hou, C.-H.; Taboada-Serrano, P.; Yiacoumi, S.; Tsouris, C. Electrosorption Selectivity of Ions from Mixtures of Electrolytes inside Nanopores. *J. Chem. Phys.* **2008**, *129* (22), 224703. https://doi.org/10.1063/1.3033562.
(53) Pawlowicz, R. Calculating the Conductivity of Natural Waters. *Limnol. Oceanogr. Methods* **2008**, *6* (9), 489–501. https://doi.org/10.4319/lom.2008.6.489.
(54) Gabelich, C. J.; Tran, T. D.; Suffet, I. H. "Mel." Electrosorption of Inorganic Salts from Aqueous Solution Using Carbon Aerogels. *Environ. Sci. Technol.* **2002**, *36* (13), 3010–3019. https://doi.org/10.1021/es0112745.